

[Click here to view linked References](#)

1 **Title:** Changes in the intra- and peri-cellular sclerostin distribution in lacuno-canalicular system  
2 induced by mechanical unloading

3 Ryuta Osumi<sup>1, #</sup>, Ziyi Wang<sup>2, 3, #</sup>, Yoshihito Ishihara<sup>1</sup>, Naoya Odagaki<sup>1</sup>, Tadahiro Iimura<sup>4</sup>, Hiroshi  
4 Kamioka<sup>2\*</sup>

5 **Affiliation:**

6 <sup>1</sup>Department of Orthodontics, Okayama University Hospital, Japan

7 <sup>2</sup>Department of Orthodontics, Graduate School of Medicine, Dentistry and Pharmaceutical  
8 Sciences, Okayama University, Japan

9 <sup>3</sup>Research Fellow of Japan Society for the Promotion of Science, Tokyo, Japan

10 <sup>4</sup>Hokkaido University, Graduate School of Dental Medicine Department of Pharmacology, Japan

11 #The first two authors contributed equally to this work.

12 **\*Corresponding author**

13 Hiroshi Kamioka<sup>1\*</sup>

14 Department of Orthodontics,

15 Okayama University Graduate School of Medicine, Dentistry, and Pharmaceutical Sciences

16 2-5-1 Shikata-cho, Okayama City, Okayama, 700-8558, JAPAN

17 **Tel:** +81 86 2356690 / **Fax:** +81 86 2356694

18 **E-mail:** [kamioka@md.okayama-u.ac.jp](mailto:kamioka@md.okayama-u.ac.jp)

19 **Keywords** Sclerostin distribution • Lacuno-canalicular system • Mechanical unloading

20 **Compliance with ethical standards**

21 **Conflict of interest** All authors have no conflict of interest.

22 **Ethical approval** This study did not involve human participants.

23 **Informed consent** This study does not involve human participants and, therefore, does not require  
24 informed consent.

25 **Abstract**

26 **Background:** Mechanical stimuli regulate Sclerostin (Scl), a negative regulator of bone formation,  
27 expression in osteocytes. However, the detailed Scl distribution in osteocytes in response to  
28 mechanical unloading remains unclear.

29 **Methods:** Twelve-week-old male rats were used. The sciatic and femoral nerves on the right side  
30 were excised as mechanical unloading treatment. A sham operation was performed on the left side.  
31 One week after neurotrauma, the bone density of the femora was evaluated by peripheral  
32 quantitative computed tomography, and immunofluorescence was performed in coronal sections  
33 of the femoral diaphysis. The mean fluorescence intensity and fluorescent profile of Scl from the  
34 marrow to the periosteal side were analyzed to estimate the Scl expression and determine to which  
35 side (marrow or periosteal) the Scl prefers to distribute in response to mechanical unloading. The  
36 most sensitive region indicated by the immunofluorescence results was further investigated by  
37 transmission electron microscopy (TEM) with immunogold staining to show the Scl expression  
38 changes in different subcellular structures.

39 **Results:** In femur distal metaphysis, neurotrauma-induced mechanical unloading significantly  
40 decreased the bone density, made the distribution of Scl closer to the marrow on the anterior and  
41 medial side, and increased the Scl expression only on the lateral side. TEM findings showed that  
42 only the expression of Scl in canaliculi was increased by mechanical unloading.

43 **Conclusion:** Our results showed that even short-term mechanical unloading is enough to decrease  
44 bone density, and mechanical unloading not only regulated the Scl expression but also changed  
45 the Scl distribution in both the osteocyte network and subcellular structures.

46 **Introduction**

47 Mechanical unloading (reduced mechanical stress on the bone) induces significant bone loss, as  
48 evidenced by disuse osteoporosis, which is a critical issue for bedridden patients and astronauts  
49 [1, 2]. Mechanical loading is a crucial factor controlling bone mass [2].

50 Osteocytes are thought to be the major bone cell type responsible for sensing mechanical  
51 loading and orchestrating signals of bone resorption and formation [1, 3]. Osteocytes are former  
52 osteoblasts that become surrounded by unmineralized matrix during bone formation; they make  
53 up 90%-95% of the adult bone cell population [4]. They form a three-dimensional (3D) structural  
54 network and are extensively coupled to each other via their slender cell process [5, 6]. Osteocytes  
55 are proposed to play a significant role in bone mechanosensation based on their location and  
56 typical morphology [7, 8].

57 Sclerostin (Scl, SOST) is a protein encoded by the *SOST* gene that is primarily secreted by  
58 osteocytes and is known to be a negative regulator of the bone mass [8, 9]. Scl binds to low-  
59 density lipoprotein receptor-related proteins (LRP) 5, LRP 6, and frizzled receptors to antagonize  
60 Wnt/ $\beta$ catenin signaling [10–13]. Wnt/ $\beta$ catenin signaling is crucial for osteoblast differentiation.  
61 Therefore, Scl inhibits bone formation [14–20].

62 *SOST* knockout mice have an extremely high bone mass, similar to that found in cases of  
63 sclerosis and Van Buchem's disease, which are genetic diseases in humans resulting from the  
64 complete absence of active sclerostin caused by a mutation in *SOST* [21, 22]. Furthermore, Scl  
65 appears to be central to the response of bone to mechanical loading [20]. The Scl expression  
66 increases with mechanical unloading and decreases with mechanical loading [16, 20, 23, 24].  
67 Furthermore, in mechanically loaded cortical bone, Scl is localized inside the osteocyte cell body.  
68 In contrast, in unloaded cortical bone, Scl is distributed not only inside the osteocyte cell body but  
69 also in the lacuno-canalicular network [16]. The distinct local expression pattern of Scl by  
70 osteocytes may contribute to the site-specific activity of bone turnover, thus ultimately regulating  
71 local modeling and remodeling [17]. However, the mechanism underlying this change is unclear,

72 as mature osteocytes mainly produce Scl [25, 26].

73 Mature osteocytes are characterized by few cytoplasmic organelles [27]. Therefore, it might  
74 be difficult to attribute the significant change in the Scl distribution only to changes in the Scl  
75 production. Furthermore, the details concerning the Scl distribution in osteocytes by mechanical  
76 unloading remain unclear.

77 Age-related cortical thinning is mainly caused by endocortical resorption [28]. In addition,  
78 previous studies [29, 30] have reported a higher response to loading at the endocortical surface  
79 than the periosteal surface. However, a study including a finite element analysis showed that the  
80 greater response to loading at the endocortical surface is not due to the endocortical surface  
81 receiving more mechanical stimuli [31].

82 In the present study, we hypothesized that mechanical unloading induced changes in not only  
83 the Scl expression but also the distribution of Scl. To observe the inter- and sub-cellular Scl  
84 distribution in the osteocytic lacuno-canalicular system, we performed immunogold staining with  
85 transmission electron microscopy (TEM). However, the region that we were able to observe by  
86 TEM was quite small. We had to observe a wide area of the bone tissue in order to detect the  
87 region that was sensitive to mechanical loading. Therefore, before performing TEM observation,  
88 we conducted immunofluorescent staining and observed the bone tissue with a confocal laser  
89 scanning microscopy system. After identifying the regions showing significant mechanical  
90 unloading-induced changes in the Scl expression, we observed the osteocytes in those regions by  
91 TEM. We then analyzed the precise Scl distribution in osteocytes under loading and unloading  
92 conditions.

## 93 **Materials and Methods**

### 94 *Animals*

95 All animal experimental protocols were conducted in accordance with the guidelines of the animal  
96 care and use committee of Okayama University (OKU-2016367). Ten male, 12-week old Sprague  
97 Dawley rats were purchased from Japan SLC (Shizuoka, Japan). Rats were kept at 21-24 °C and  
98 given free access to water and food.

### 99 *Experimental design*

100 After isoflurane-induced anesthesia, as shown in **Figure 1A upper panel**, rats received an  
101 approximately 2-cm incision on the right thigh, and the fascia was incised. The sciatic nerve was  
102 then dissected out and excised to about 5 mm. Also, an approximately 2-cm incision was made at  
103 the right inguinal region (**Fig. 1A lower panel**), and the femoral nerve was dissected out and  
104 excised to about 5 mm (NX group: unloading condition). On the opposite side, the sciatic and  
105 femoral nerves were exposed but were not excised, as a sham operation (sham group: loading  
106 condition). Since the sciatic nerve controls the muscle of the flexor of the posterior region of the  
107 femur and the femoral nerve controls the muscle of the anterior region, excising both the sciatic  
108 and femoral nerves fully immobilized the target leg.

### 109 *Sample preparation*

110 Seven days after surgery, anesthetized rats were perfused and fixed with 4% paraformaldehyde in  
111 phosphate-buffered saline (PFA/PBS), and their right and left femurs were dissected. Femurs were  
112 immersed in 17% EDTA (OSTEOSOFT; Merck Millipore, Burlington, MA, USA) for 28 days at  
113 4 °C for demineralization. Samples for immunohistochemistry were embedded in paraffin and cut  
114 into 7- $\mu$ m-thick coronal sections. Serial sections were collected onto silane-coated slides. Samples  
115 for immunogold staining were embedded in LR-White (London Resin Company Ltd., London,  
116 UK) and cut into 90-nm-thick sections.

117 ***Bone density measurement by peripheral quantitative computed tomography (pQCT)***

118 The bone density of the femoral diaphysis and distal metaphysis (3.0 mm mesial from growth  
119 plate) was analyzed by pQCT (XCT Research SA+; Stratec Medizintechnik GmbH, Pforzheim,  
120 Germany). Femurs were scanned with 0.46-mm slice thickness and 0.12-mm voxel size. Analyses  
121 were performed using the XCT 6.20 software program (Stratec Medizintechnik GmbH). The  
122 femoral contour was detected by Contour mode 2. The following definitions were used: cancellous  
123 bone corresponded to regions with 35% of the total cross-sectional area having a relatively low  
124 density (defined by Peel mode 20), while cortical bone corresponded to regions with a density of  
125 over 690 mg/cm<sup>3</sup> (defined by Cortical mode 1). The bone density measurement by pQCT was  
126 performed by Kureha analysis center Co, Ltd., Tokyo, Japan.

127 ***Immunofluorescence studies of paraffin-embedded sections***

128 Sections of femoral diaphysis were blocked in universal blocking reagent (Nacalai Tesque, Kyoto,  
129 Japan) before incubation with a goat polyclonal antibody against *SOST*/Sclerostin (AF1589; R&D  
130 Systems, Minneapolis, MN, USA; 1:200) at 4 °C overnight, followed by a species-matched Alexa  
131 Fluor 488-conjugated (Molecular Probes, Eugene, OR, USA; 1:200) secondary antibody at room  
132 temperature for 1-h. For negative controls, nonimmunized goat IgG was used as a substitute for  
133 the primary antibody. Nuclei were stained using 4',6-diamidino-2-phenylindole (DAPI; Sigma  
134 Aldrich, St. Louis, MO, USA). After rinsing the samples, the samples were embedded in  
135 fluorescence mounting medium (Dako, Carpinteria, CA, USA).

136 ***Confocal fluorescence tiling imaging***

137 Confocal tiling imaging for the immunostained femur sections was performed with an LSM 780  
138 confocal laser scanning microscopy system (CarlZeiss, Oberkochen, Germany) and C-  
139 Apochromat (63x/1.20 W Korr M27) and Plan-Apochromat (20x/0.8 M27) at Central Research  
140 Laboratory, Okayama University Medical School, Japan. Two laser lines of 405 nm and 488 nm  
141 were used. Images of 1.25 μm/pixel and 12-bit color depth were acquired.

142 ***Quantification of Scl distribution on immunofluorescence images***

143 We then divided the above-mentioned stitched fluorescence image into anterior, posterior, medial,  
144 and lateral regions (**Fig. 1B**). The fluorescence intensity was measured from the bone marrow side  
145 to the periosteum side of the cortical bone with a width of 400  $\mu\text{m}$ . We constructed mean profiles  
146 by averaging the fluorescence intensity (**Fig. 1C-1**) that perpendicular to the arrow indicated in  
147 each ROI region in **Fig. 1B**. Those profiles were then converted to a curve of the distribution  
148 tendency (**Fig. 1C-1**) using an empirical mode decomposition (EMD) method [32]. EMD was  
149 performed using “EMD” and “pracma” software packages in the R program language. The  
150 resource R script for processing our data in this study can be checked in the author’s GitHub  
151 (<https://github.com/wong-ziyi/Eccentricity>). As shown in **Fig. 1C**, this EMD method could  
152 identify the peak of the Scl distribution tendency and avoid the influence of outliers in the original  
153 profiles of fluorescence intensity (**Fig. 1C-1**). Eccentricity was defined as  $\text{Eccentricity} = (2S -$   
154  $L)/L$ , where S is the location of the peak of the distribution tendency, and L is the total length of  
155 the ROI region. Since we set the boundary of the marrow as 0, positive eccentricity indicates that  
156 the peak of the Scl distribution tendency is closer to the marrow side, while negative eccentricity  
157 indicates that it is closer to the periosteal side. The number of cells with positive staining for Scl  
158 was analyzed using the “Analyze Particles” function after auto-thresholding with the default  
159 method using the ImageJ/Fiji software program (US National Institute of Health, Bethesda, MD,  
160 USA).

161 ***3D image construction***

162 The 3D immunofluorescence images were constructed from the z-series of CLS images using the  
163 IMARIS software program (Bitplane, Zurich, Switzerland) as described previously [17, 33].

164 ***Immunolectron microscopy and quantification of the Scl distribution***

165 Ultrathin sections were etched in 0.05 M glutaraldehyde and 6 M urea for 10 minutes. After  
166 rinsing, the sections were blocked in 1% bovine serum albumin and 10% rabbit serum for 15

167 minutes. Sections were incubated with goat polyclonal antibody against *SOST*/Sclerostin  
168 (AF1589; R&D Systems) (1:100) at 4 °C overnight, followed by a rabbit anti-goat IgG conjugated  
169 with 10-nm colloidal gold (EMARG10; BBI Solutions, Crumlin, UK) (1:50) secondary antibody  
170 at room temperature for 2-h. After washing, the samples were fixed with 1% glutaraldehyde and  
171 then observed and photographed via TEM (H7650; HITACHI, Tokyo, Japan) at Central Research  
172 Laboratory, Okayama University Medical School. The Scl distribution was evaluated by  
173 calculating the Scl density per unit area of the osteocyte cell body, lacuna, and canaliculi. Acquired  
174 images were analyzed using the Image J software program.

### 175 ***Statistical analyses***

176 A paired *t*-test was applied to determine the significant difference between the sham and NX group.  
177 We performed two-way analyses of variance (ANOVAs) with paired samples to test whether or  
178 not an interaction effect between NX and position existed. The followed Fisher's Least Significant  
179 Difference with a single pooled variance was performed for multiple comparisons among different  
180 regions (anterior, posterior, medial, and lateral regions for immunostaining images and the cell  
181 body, lacuna, and canaliculi for TEM images) in each treatment group (sham or NX).

182 In the above statistical analyses, measurements at  $P < 0.05$  were considered statistically  
183 significant. All data are expressed as the mean  $\pm$  standard deviation (SD).

184 All of these statistical analyses were performed using either the GraphPad Prism 6 software  
185 program (GraphPad Software, Inc., San Diego, CA, USA) or the R software program  
186 (<https://www.R-project.org/>).



187 **Results**

188 *The bone density is decreased in the distal metaphysis of the femur under unloading conditions*

189 After fully immobilizing (please check the rat's ambulatory in **Online Resource 1**) the right leg  
190 seven days, pQCT showed that, in the distal metaphysis of the femur, the total bone density,  
191 cortical bone density, and cancellous bone density were decreased in the NX group (**Fig. 2A**). In  
192 contrast, no significant changes in the femoral diaphysis were noted between the sham and NX  
193 groups (**Fig. 2B**).

194 *Mechanical unloading significantly changed the Scl expression in the lateral and medial  
195 regions of the femoral diaphysis.*

196 According to the two-way ANOVA, dissection of the femoral nerve (NX) contributed to 11.74%  
197 and 20.18% of the total variance for the NX-induced changes in the Scl distribution (**Fig. 2C**  
198 **upper panel**) and expression (**Fig. 2C lower panel**), respectively. The upper panel of **Fig. 2C**  
199 showed that NX-induced unloading brought the distribution of Scl significantly closer to the  
200 marrow on the anterior and medial side, while the expression of Scl was significantly increased  
201 by NX-induced unloading only on the lateral side (**Fig. 2C lower panel**). No interaction effect  
202 was observed in the Scl distribution (**Fig. 2C upper panel**) or expression (**Fig. 2C lower panel**).

203 Interestingly, the Scl distribution differed among the four regions in the Sham group. The Scl  
204 distribution in the anterior and medial regions was closer to the periosteal side than that in the  
205 posterior and lateral regions (**Fig. 2C upper panel**). However, there were no significant  
206 differences in the eccentricity in any region in the NX group (**Fig. 2C upper panel**). These results  
207 imply that the lateral region is sensitive to mechanical loading.

208 *The location closest to the periosteum in the lateral region of the femoral diaphysis is where  
209 the Scl distribution is likely to change due to mechanical unloading*

210 As shown in **Fig. 3A**, we divided the lateral region into four equal parts ( I, II, III, and IV) to  
211 identify the region most drastically changed in response to unloading for further TEM observation.

212 We counted the number of Scl-positive osteocytes and calculated the ratio of Scl-positive  
213 osteocytes to total osteocytes in each of the four parts (**Fig. 3C**). There were significantly more  
214 Scl-positive osteocytes in part IV of the NX group than in the Sham group (**Fig. 3C**). When  
215 checking 3D images of Scl immunofluorescence, we noted dynamic changes in the Scl  
216 distribution in the osteocytic lacuna-canalicular system in part IV (**Fig. 3D**), which was further  
217 confirmed by TEM observations.

218 ***The mechanical unloading increased the Scl expression only in the canaliculi***

219 Since most changes in the Scl expression were observed in part IV of the lateral region, as  
220 mentioned above, the subsequent TEM observation was focused on this specific site. Using  
221 immunoelectron microscopy, we observed the Scl distribution inside the osteocyte cell body,  
222 lacuna, and canaliculi (**Fig. 4A**). We counted the Scl molecules labeled by 10-nm colloidal gold  
223 and measured the density per square micrometer in the osteocyte cell body, lacuna, and canaliculi  
224 (**Fig. 4B upper panel**). The Scl density was significantly higher in the canaliculi of the NX group  
225 than in the Sham group. We also analyzed the differences in the Scl density in canaliculi, lacuna,  
226 and cell body between the Sham and NX groups. In the Sham group, the Scl density was higher  
227 in the canaliculi than in the lacuna, while no significant difference in the Scl density was noted  
228 between the cell body and lacuna or canaliculi (**Fig. 4B upper panel**). In the NX group, the Scl  
229 density was significantly higher in the canaliculi than in the cell body or lacuna, with no significant  
230 difference noted between the cell body and lacuna. Although a two-way ANOVA showed a  
231 significant contribution of both the position and NX, there was no significant interaction effect  
232 between the position and NX (**Fig. 4B upper panel**).

233 Intriguingly, NX-induced mechanical unloading did not induce any significant area changes  
234 in the cell body, lacuna, or canaliculi. Indeed, a two-way ANOVA analysis also showed that NX  
235 had no significant contribution to the area difference (**Fig. 4B lower panel**). Notably, there was  
236 no marked in the density of Scl between cell bodies and their respective lacunae.

237 **Discussion**

238 The present study aimed to analyze the Scl distribution in osteocytes under loading and unloading  
239 conditions. Furthermore, we considered whether or not Scl transportation was related to changes  
240 in its distribution.

241 We prepared an animal model of disuse osteoporosis. First, using confocal laser scanning  
242 microscopy, we observed a wide region of the femur section immunolabeled with an antibody  
243 against SOST/sclerostin. We then detected the regions where the change in the Scl distribution  
244 was sensitive to mechanical loading. Second, in those same regions, we labeled anti-Scl antibody  
245 with 10-nm gold colloid and observed osteocytes using TEM. In contrast to the rodent models of  
246 disuse osteoporosis that have been generated via tail suspension and neurectomy of the lower hind  
247 limb [16, 19], in the present study, we performed unilateral neurectomy to obtain mechanically  
248 loaded and unloaded cortical bone in the same rat. The results of pQCT showed that the density  
249 of cortical bone and cancellous bone in the distal metaphysis of the femur was significantly  
250 decreased under unloading conditions, as previously described [34]. Therefore, our study of  
251 mechanical unloading in an animal model was well controlled.

252 Osteocytes reportedly tend to align themselves in the direction of the principle mechanical  
253 loading direction [35, 36]. The difference in the orientation of the osteocyte cell bodies in  
254 cancellous bone of the femur between loaded and unloaded conditions is not as significant as  
255 those detected in the cortical bone of the femoral midshaft. A previous computer simulation study  
256 reported that the external forces exerted on the cortical bone were greater than those exerted on  
257 cancellous bone [37]. Femoral diaphysis is suitable for observing the loading-related strain  
258 distribution [16]. We therefore performed immunofluorescence staining in coronal sections of the  
259 femoral diaphysis. Different positions (anterior, posterior, lateral, or medial) did not contribute  
260 significantly to the variance of the Scl distribution, and no interaction effect was observed on a  
261 two-way ANOVA (**Fig. 2C lower panel**), which suggested that the changes in the peak of the Scl  
262 distribution tendency were mainly due to the NX-induced mechanical unloading. In the lateral

263 and anterior regions, the peak of the Scl distribution tendency shifted to the region adjacent to the  
264 marrow under NX-induced mechanical unloading (**Fig. 2C upper panel**). However, only the  
265 lateral region showed significant changes in the fluorescence intensity between the Sham and NX  
266 groups, with no such changes noted in the anterior, posterior, or medial regions (**Fig. 2C lower**  
267 **panel**).

268 We then divided the lateral region into four parts to analyze the Scl distribution in more detail  
269 by identifying Scl-expressing cells (**Fig. 3A**). In the lateral region of the NX group, the Scl-  
270 expressing cell count was higher than in the Sham group in the area closest to the periosteum (**Fig.**  
271 **3C**). These results imply that loading induced the most marked changes in the Scl distribution in  
272 the periosteal side of the lateral regions. We then constructed 3D images to analyze the Scl  
273 distribution around osteocytes, with the images showing that Scl was localized to a narrow area  
274 under loading conditions but spread more broadly under unloading conditions.

275 Next, in the same regions, we analyzed the Scl distribution inside the osteocyte cell body,  
276 lacuna, and canaliculi under loading and unloading conditions via immunogold staining with TEM.  
277 There were no significant differences in the Scl density inside the cell body and lacuna between  
278 the NX and Sham groups (**Fig. 4B upper panel**). However, the Scl density inside the canaliculi  
279 was significantly higher in the NX group than in the Sham group (**Fig. 4B upper panel**). In the  
280 NX group, the Scl density was significantly higher inside the canaliculi than inside the osteocyte  
281 cell body or lacuna (**Fig. 4B upper panel**). According to the two-way ANOVA, different positions  
282 (cell body, lacuna, or canaliculi) contributed the most to the variance in the Scl expression.  
283 However, no interaction effect was observed, which suggested that the mechanical unloading-  
284 induced changes in the Scl expression were site-specific (**Fig. 4B upper panel**). Those findings  
285 indicated that the Scl expression was denser in the canaliculi than at other sites (i.e., cell body and  
286 lacuna), and the expression in the canaliculi was more sensitive to mechanical unloading than that  
287 at other sites. Those findings are consistent to our previous report that the mechanosensitivity of  
288 the cell processes was higher than that of the cell body in osteocyte [38].

289 As shown in the upper panel of **Fig. 2C**, Scl distributed more to the marrow side in the  
290 anterior and medial regions of the NX group than the Sham group. In addition, the anterior and  
291 medial regions were more sensitive to NX-induced mechanical unloading than posterior or lateral  
292 regions since the peak of Scl distribution tendency was shifted from the periosteal side to the  
293 marrow side (**Fig. 2C upper panel**). However, the overall expression of Scl indicated by the  
294 fluorescence in **Fig. 2C lower panel** was unchanged. These findings suggested that Scl  
295 distribution was more sensitive to mechanical stimuli than the Scl expression. In other words,  
296 solute transport is more sensitive to mechanical stimuli-induced expression changes than Scl  
297 synthesis. Consistent with our findings, based on the finite element analysis, a previous report  
298 found that the endocortical surface showed a greater response to loading but received less  
299 mechanical stimuli [31]. The changes in the Scl distribution among osteocytes observed in the  
300 present study may explain this paradox [31]. Indeed, our findings suggest a possible “energy”-  
301 saving strategy for bone in response to mechanical stimuli, since the relative concentration of Scl  
302 was increased near the marrow side (**Fig. 2C upper panel**). However, the overall concentration  
303 may not have been changed (**Fig. 2C lower panel**) under NX-induced mechanical unloading.

304 Our TEM results showed that the Scl density in the osteocyte cell body and lacuna did not  
305 differ markedly between the Sham and NX groups (**Fig. 4**), which showed a relatively high  
306 concentration of sclerostin in the lacuno-canalicular system outside of osteocytes. Our previous  
307 study [39] suggested that the fluid flow profile in the lacuno-canalicular system is determined by  
308 the morphology of the canalicular wall. However, the morphology of the lacuno-canalicular  
309 system is susceptible to being changed by bone matrix deformation under different mechanical  
310 loading environments. Thus, the relatively high concentration of sclerostin outside of the  
311 osteocytes facilitated the re-distribution of Scl in the lacuno-canalicular system when the  
312 mechanical loading environment changed. Since transportation of Scl outside of the osteocytes in  
313 the lacuno-canaliculi occurs more rapidly than changing the Scl expression, the above may be a  
314 potential mechanism rendering Scl distribution more sensitive to mechanical stimuli than the Scl

315 expression.

316 Solute transport through the lacuno-canalicular system occurs by both diffusion and  
317 convection [40]. Diffusion depends on solute concentration gradients, while convection depends  
318 on movement through the pericellular space. Since the fluid is incompressible, the deformation of  
319 bone under mechanical loading forces it to flow (like squeezing a sponge), as demonstrated by  
320 Piekarski and Munro [41]. Forces that induce fluid flow are mainly generated by muscular actions  
321 and reactions due to physical activity [41, 42]. Solute transport in the lacuno-canalicular system  
322 is dependent on the size of the molecules, with small solutes under 1 kDa or roughly 1 nm in  
323 diameter (e.g., glucose and ATP) being easily transported by diffusion, while larger solutes in the  
324 range of 10-70 kDa or up to 6 nm in diameter (e.g., Scl, *RANKL* and parathyroid hormone) require  
325 convective transportation [43–47].

### 326 **Limitations**

327 In the present study, the area of the cell body, lacuna, and canaliculi did not show any marked  
328 differences between the Sham and NX group, which suggested that we did not observe any  
329 osteocytic osteolysis that was recently confirmed in lactation [48], space flight [49], and hindlimb  
330 suspension [50] mouse models. The treatment duration (seven days) in this study was shorter than  
331 that in those previous reports (two to three weeks) that observed osteocytic osteolysis, so  
332 osteocytic osteolysis may not be an early response to mechanical unloading. Alternatively, this  
333 discrepancy may have been due to the femoral and sciatic nerve dissection performed in this study,  
334 as emerging evidence has indicated that innervation is important for bone remodeling [51].  
335 However, the underlying mechanism will need to be explored in further investigations.

### 336 **Summary**

337 Our results showed that even a short-term (seven days) mechanical unloading was able to  
338 decrease the bone density (**Fig. 2A**). However, the Scl distribution showed more significant  
339 changes than the Scl expression (**Fig. 2C** and **Fig. 3**), possibly due to a relative high concentration  
340 of Scl outside of osteocytes in lacuno-canaliculi (**Fig. 4**). Interestingly, the short-term mechanical

341 unloading in the present study increased the Scl expression only in the canaliculi (**Fig. 4B upper**  
342 **panel**), and the unchanged area in subcellular structures indicated no osteocytic osteolysis (**Fig.**  
343 **4B lower panel**).

344 The present findings suggested that, given the relatively high concentration of Scl outside of  
345 osteocytes in the lacuno-canaliculi, changes in the Scl distribution in both the osteocyte network  
346 and subcellular structures were early events in response to neurotrauma-induced mechanical  
347 unloading. Given the findings of previous studies, early changes in the Scl distribution may play  
348 a crucial role in the bone's response to mechanical stimuli, which should be further explored in  
349 future investigations.

#### 350 **Author Contributions**

351 H.K., R.O., T.I., and Z.W. designed the study. R.O., N.O., T.I., and Y.I. conducted the study. Z.W.  
352 tested the existing code components, programmed script for data processing, and drew the sketch.  
353 R.O. and Z.W. processed, analyzed, and visualized the data and wrote the manuscript. R.O., Z.W.,  
354 T.I., Y.I., and H.K. interpreted the data and approved the final version of the manuscript. H.K. is  
355 responsible for the integrity of the data analysis. R.O and Z.W. contributed equally to this work.

#### 356 **Acknowledgments**

357 The authors would like to thank Masumi Furutani and Megumi Tsukano, Central Research  
358 Laboratory, Okayama University Medical School, for their technical assistance in this study. This  
359 work was supported by a Grant-in-Aid for Scientific Research (to T. Iimura [18H02983], Y.  
360 Ishihara [17H04413], Z. Wang [19J1190611] and H. Kamioka [16H05549, 19H03859]) from the  
361 Japan Society for the Promotion of Science, Japan.

362 **References**

- 363 1. Fu S, Kuwahara M, Uchida Y, et al (2019) Circadian production of melatonin in cartilage  
364 modifies rhythmic gene expression. *J Endocrinol* 241:161–173.  
365 <https://doi.org/10.1530/JOE-19-0022>
- 366 2. Keune JA, Branscum AJ, Iwaniec UT, Turner RT (2016) Effects of Spaceflight on Bone  
367 Microarchitecture in the Axial and Appendicular Skeleton in Growing Ovariectomized  
368 Rats. *Sci Rep* 5:18671. <https://doi.org/10.1038/srep18671>
- 369 3. Kogawa M, Khalid KA, Wijenayaka AR, et al (2018) Recombinant sclerostin antagonizes  
370 effects of ex vivo mechanical loading in trabecular bone and increases osteocyte lacunar  
371 size. *Am J Physiol Physiol* 314:C53–C61. <https://doi.org/10.1152/ajpcell.00175.2017>
- 372 4. Schaffler MB, Cheung W-Y, Majeska R, Kennedy O (2014) Osteocytes: Master  
373 Orchestrators of Bone. *Calcif Tissue Int* 94:5–24. [https://doi.org/10.1007/s00223-013-](https://doi.org/10.1007/s00223-013-9790-y)  
374 [9790-y](https://doi.org/10.1007/s00223-013-9790-y)
- 375 5. Kamioka H, Honjo T, Takano-Yamamoto T (2001) A three-dimensional distribution of  
376 osteocyte processes revealed by the combination of confocal laser scanning microscopy  
377 and differential interference contrast microscopy. *Bone* 28:145–149.  
378 [https://doi.org/10.1016/S8756-3282\(00\)00421-X](https://doi.org/10.1016/S8756-3282(00)00421-X)
- 379 6. Ishihara Y, Kamioka H, Honjo T, et al (2008) Hormonal, pH, and calcium regulation of  
380 connexin 43-mediated dye transfer in osteocytes in chick calvaria. *J Bone Miner Res*  
381 23:350–60. <https://doi.org/10.1359/jbmr.071102>



- 382 7. Bonewald LF (2011) The amazing osteocyte. *J Bone Miner Res* 26:229–238.  
383 <https://doi.org/10.1002/jbmr.320>
- 384 8. Sugawara Y, Kamioka H, Ishihara Y, et al (2013) The early mouse 3D osteocyte network  
385 in the presence and absence of mechanical loading. *Bone* 52:189–196.  
386 <https://doi.org/10.1016/j.bone.2012.09.033>
- 387 9. Williams DK, Parham SG, Schryver E, et al (2018) Sclerostin Antibody Treatment  
388 Stimulates Bone Formation to Normalize Bone Mass in Male Down Syndrome Mice.  
389 *JBMR Plus* 2:47–54. <https://doi.org/10.1002/jbm4.10025>
- 390 10. Delgado-Calle J, Sato AY, Bellido T (2017) Role and mechanism of action of sclerostin in  
391 bone. *Bone* 96:29–37. <https://doi.org/10.1016/j.bone.2016.10.007>
- 392 11. Odagaki N, Ishihara Y, Wang Z, et al (2018) Role of Osteocyte-PDL Crosstalk in Tooth  
393 Movement via SOST/Sclerostin. *J Dent Res* 97:1374–1382.  
394 <https://doi.org/10.1177/0022034518771331>
- 395 12. Nicol L, Wang Y, Smith R, et al (2018) Serum Sclerostin Levels in Adults With  
396 Osteogenesis Imperfecta: Comparison With Normal Individuals and Response to  
397 Teriparatide Therapy. *J Bone Miner Res* 33:307–315. <https://doi.org/10.1002/jbmr.3312>
- 398 13. Anagnostis P, Vakilopoulou S, Christoulas D, et al (2018) The role of sclerostin/dickkopf-  
399 1 and receptor activator of nuclear factor kB ligand/osteoprotegerin signalling pathways in  
400 the development of osteoporosis in patients with haemophilia A and B: A cross-sectional  
401 study. *Haemophilia* 24:316–322. <https://doi.org/10.1111/hae.13384>

- 402 14. Kramer I, Halleux C, Keller H, et al (2010) Osteocyte Wnt/ $\beta$ -Catenin Signaling Is Required  
403 for Normal Bone Homeostasis. *Mol Cell Biol* 30:3071–3085.  
404 <https://doi.org/10.1128/MCB.01428-09>
- 405 15. Kennedy OD, Herman BC, Laudier DM, et al (2012) Activation of resorption in fatigue-  
406 loaded bone involves both apoptosis and active pro-osteoclastogenic signaling by distinct  
407 osteocyte populations. *Bone* 50:1115–1122. <https://doi.org/10.1016/j.bone.2012.01.025>
- 408 16. Moustafa A, Sugiyama T, Prasad J, et al (2012) Mechanical loading-related changes in  
409 osteocyte sclerostin expression in mice are more closely associated with the subsequent  
410 osteogenic response than the peak strains engendered. *Osteoporos Int* 23:1225–1234.  
411 <https://doi.org/10.1007/s00198-011-1656-4>
- 412 17. Watanabe T, Tamamura Y, Hoshino A, et al (2012) Increasing participation of sclerostin in  
413 postnatal bone development, revealed by three-dimensional immunofluorescence  
414 morphometry. *Bone* 51:447–458. <https://doi.org/10.1016/j.bone.2012.06.019>
- 415 18. Yavropoulou M, Xygonakis C, Lolou M, et al (2014) The sclerostin story: From human  
416 genetics to the development of novel anabolic treatment for osteoporosis. *Hormones*  
417 13:476–487. <https://doi.org/10.14310/horm.2002.1552>
- 418 19. Lv J, Sun X, Ma J, et al (2015) Involvement of periostin–sclerostin–Wnt/ $\beta$ -catenin  
419 signaling pathway in the prevention of neurectomy-induced bone loss by naringin.  
420 *Biochem Biophys Res Commun* 468:587–593. <https://doi.org/10.1016/j.bbrc.2015.10.152>
- 421 20. Spatz JM, Wein MN, Gooi JH, et al (2015) The Wnt inhibitor sclerostin is up-regulated by

- 422 mechanical unloading in osteocytes in vitro. *J Biol Chem* 290:16744–16758.  
423 <https://doi.org/10.1074/jbc.M114.628313>
- 424 21. Sebastian A, Loots GG (2018) Genetics of Sost/SOST in sclerosteosis and van Buchem  
425 disease animal models. *Metabolism* 80:38–47.  
426 <https://doi.org/10.1016/j.metabol.2017.10.005>
- 427 22. Albiol L, Cilla M, Pflanz D, et al (2018) Sost deficiency leads to reduced mechanical strains  
428 at the tibia midshaft in strain-matched in vivo loading experiments in mice. *J R Soc*  
429 *Interface* 15:20180012. <https://doi.org/10.1098/rsif.2018.0012>
- 430 23. Suzuki N, Aoki K, Marcián P, et al (2016) A threshold of mechanical strain intensity for  
431 the direct activation of osteoblast function exists in a murine maxilla loading model.  
432 *Biomech Model Mechanobiol* 15:1091–1100. <https://doi.org/10.1007/s10237-015-0746-1>
- 433 24. Galea GL, Lanyon LE, Price JS (2017) Sclerostin's role in bone's adaptive response to  
434 mechanical loading. *Bone* 96:38–44. <https://doi.org/10.1016/j.bone.2016.10.008>
- 435 25. Poole KES, Van Bezooijen RL, Loveridge N, et al (2005) Sclerostin is a delayed secreted  
436 product of osteocytes that inhibits bone formation. *FASEB J* 19:1842–1844.  
437 <https://doi.org/10.1096/fj.05-4221fje>
- 438 26. Sebastian A, Loots GG (2017) Transcriptional control of Sost in bone. *Bone* 96:76–84.  
439 <https://doi.org/10.1016/j.bone.2016.10.009>
- 440 27. Irie K, Ejiri S, Sakakura Y, et al (2008) Matrix Mineralization as a Trigger for Osteocyte  
441 Maturation. *J Histochem Cytochem* 56:561–567. <https://doi.org/10.1369/jhc.2008.950527>

- 442 28. Neu CM, Rauch F, Manz F, Schöenau E (2001) Modeling of Cross-sectional Bone Size,  
443 Mass and Geometry at the Proximal Radius: A Study of Normal Bone Development Using  
444 Peripheral Quantitative Computed Tomography. *Osteoporos Int* 12:538–547.  
445 <https://doi.org/10.1007/s001980170074>
- 446 29. Grimston SK, Brodt MD, Silva MJ, Civitelli R (2008) Attenuated Response to In Vivo  
447 Mechanical Loading in Mice With Conditional Osteoblast Ablation of the Connexin43  
448 Gene (*Gja1*). *J Bone Miner Res* 23:879–886. <https://doi.org/10.1359/jbmr.080222>
- 449 30. Brodt MD, Silva MJ (2010) Aged mice have enhanced endocortical response and normal  
450 periosteal response compared with young-adult mice following 1 week of axial tibial  
451 compression. *J Bone Miner Res* 25:2006–2015. <https://doi.org/10.1002/jbmr.96>
- 452 31. Birkhold AI, Razi H, Duda GN, et al (2016) The Periosteal Bone Surface is Less Mechano-  
453 Responsive than the Endocortical. *Sci Rep* 6:23480. <https://doi.org/10.1038/srep23480>
- 454 32. Huang N, Shen Z, Long S, et al (1998) The empirical mode decomposition and the Hilbert  
455 spectrum for nonlinear and non-stationary time series analysis. *Proc R Soc A Math Phys*  
456 *Eng Sci* 454:995, 903. <https://doi.org/10.1098/rspa.1998.0193>
- 457 33. Nishiyama Y, Matsumoto T, Lee J-W, et al (2015) Changes in the spatial distribution of  
458 sclerostin in the osteocytic lacuno-canalicular system in alveolar bone due to orthodontic  
459 forces, as detected on multimodal confocal fluorescence imaging analyses. *Arch Oral Biol*  
460 60:45–54. <https://doi.org/10.1016/j.archoralbio.2014.08.013>
- 461 34. Murakami H, Nakamura T, Tsurukami H, et al (2009) Effects of tiludronate on bone mass,

- 462 structure, and turnover at the epiphyseal, primary, and secondary spongiosa in the proximal  
463 tibia of growing rats after sciatic neurectomy. *J Bone Miner Res* 9:1355–1364.  
464 <https://doi.org/10.1002/jbmr.5650090906>
- 465 35. EJIRI S, OZAWA H (1982) Scanning Electron Microscopic Observations of Rat Tibia  
466 Using the HCl-Collagenase Method. *Arch Histol Cytol* 45:399–401.  
467 <https://doi.org/10.1679/aohc.45.399>
- 468 36. Vatsa A, Breuls RG, Semeins CM, et al (2008) Osteocyte morphology in fibula and calvaria  
469 - Is there a role for mechanosensing? *Bone* 43:452–458.  
470 <https://doi.org/10.1016/j.bone.2008.01.030>
- 471 37. Tezuka K, Wada Y, Takahashi A, Kikuchi M (2005) Computer-simulated bone architecture  
472 in a simple bone-remodeling model based on a reaction-diffusion system. *J Bone Miner*  
473 *Metab* 23:1–7. <https://doi.org/10.1007/s00774-004-0533-z>
- 474 38. Adachi T, Aonuma Y, Tanaka M, et al (2009) Calcium response in single osteocytes to  
475 locally applied mechanical stimulus: Differences in cell process and cell body. *J Biomech*  
476 42:1989–1995. <https://doi.org/10.1016/j.jbiomech.2009.04.034>
- 477 39. Kamioka H, Kameo Y, Imai Y, et al (2012) Microscale fluid flow analysis in a human  
478 osteocyte canaliculus using a realistic high-resolution image-based three-dimensional  
479 model. *Integr Biol* 4:1198–1206. <https://doi.org/10.1039/c2ib20092a>
- 480 40. Wang L, Wang Y, Han Y, et al (2005) In situ measurement of solute transport in the bone  
481 lacunar-canalicular system. *Proc Natl Acad Sci U S A* 102:11911–11916.

- 482 <https://doi.org/10.1073/pnas.0505193102>
- 483 41. Piekarski K, Munro M (1977) Transport mechanism operating between blood supply and  
484 osteocytes in long bones. *Nature* 269:80–82. <https://doi.org/10.1038/269080a0>
- 485 42. Weinbaum S, Cowin SC, Zeng Y (1994) A model for the excitation of osteocytes by  
486 mechanical loading-induced bone fluid shear stresses. *J Biomech* 27:339–360.  
487 [https://doi.org/10.1016/0021-9290\(94\)90010-8](https://doi.org/10.1016/0021-9290(94)90010-8)
- 488 43. Knothe Tate ML, Niederer P, Knothe U (1998) In vivo tracer transport through the  
489 lacunocanalicular system of rat bone in an environment devoid of mechanical loading.  
490 *Bone* 22:107–117. [https://doi.org/10.1016/S8756-3282\(97\)00234-2](https://doi.org/10.1016/S8756-3282(97)00234-2)
- 491 44. Tami AE, Schaffler MB, Knothe Tate ML (2003) Probing the tissue to subcellular level  
492 structure underlying bone's molecular sieving function. *Biorheology* 40:577–90
- 493 45. Li W, You L, Schaffler MB, Wang L (2009) The dependency of solute diffusion on  
494 molecular weight and shape in intact bone. *Bone* 45:1017–1023.  
495 <https://doi.org/10.1016/j.bone.2009.07.076>
- 496 46. Price C, Zhou X, Li W, Wang L (2011) Real-time measurement of solute transport within  
497 the lacunar-canalicular system of mechanically loaded bone: Direct evidence for load-  
498 induced fluid flow. *J Bone Miner Res* 26:277–285. <https://doi.org/10.1002/jbmr.211>
- 499 47. Wang B, Zhou X, Price C, et al (2013) Quantifying load-induced solute transport and  
500 solute-matrix interaction within the osteocyte lacunar-canalicular system. *J Bone Miner*  
501 *Res* 28:1075–1086. <https://doi.org/10.1002/jbmr.1804>

- 502 48. Qing H, Ardeshirpour L, Divieti Pajevic P, et al (2012) Demonstration of osteocytic  
503 perilacunar/canalicular remodeling in mice during lactation. *J Bone Miner Res* 27:1018–  
504 1029. <https://doi.org/10.1002/jbmr.1567>
- 505 49. Blaber EA, Dvorochkin N, Lee C, et al (2013) Microgravity Induces Pelvic Bone Loss  
506 through Osteoclastic Activity, Osteocytic Osteolysis, and Osteoblastic Cell Cycle  
507 Inhibition by CDKN1a/p21. *PLoS One* 8:e61372.  
508 <https://doi.org/10.1371/journal.pone.0061372>
- 509 50. Lloyd SA, Loisel AE, Zhang Y, Donahue HJ (2014) Evidence for the role of connexin  
510 43-mediated intercellular communication in the process of intracortical bone resorption via  
511 osteocytic osteolysis. *BMC Musculoskelet Disord* 15:122. [https://doi.org/10.1186/1471-  
512 2474-15-122](https://doi.org/10.1186/1471-2474-15-122)
- 513 51. Elefteriou F (2018) Impact of the Autonomic Nervous System on the Skeleton. *Physiol Rev*  
514 98:1083–1112. <https://doi.org/10.1152/physrev.00014.2017>

## 515 **Figure legends**

516 **Fig. 1** Experimental design and quantification method of immunofluorescence images.

- 517 (A). A schematic diagram of the excision of the sciatic and femoral nerves. LN, Lumber Nerve.  
518 (B). A schematic diagram of the scanning position for pQCT and the coronal serial sections of  
519 the midshaft of the sham and NX groups. We divided the section into anterior, posterior, medial,  
520 and lateral regions (see red dotted lines). The asterisks indicate bone marrow. The spatial  
521 immunofluorescence intensity was measured according to the direction indicated by the red  
522 arrow. (C). An example of a profile analysis. (1) The fluorescence intensity profiles of the

523 region from the bone marrow side to the periosteum side of the cortical bone (400  $\mu\text{m}$  wide).  
524 The vertical axis of the graph indicates the intensity, and the horizontal axis indicates the  
525 distance from the bone marrow side of cortical bone. “0” on the horizontal axis indicates the  
526 border between the cortical bone and periosteum. (2) The graph with one maximum value  
527 converted from the profile using empirical mode decomposition. The distance from the center  
528 of the cortical bone to the maximum value was measured. We divided the value by the distance  
529 from the bone marrow to the periosteum side and defined it as the eccentricity. Using the  
530 eccentricity as an index, we evaluated the Scl distribution

531 **Fig. 2** The findings from pQCT and immunofluorescence showing the NX-induced changes in the  
532 femoral bone density and sclerostin distribution, respectively.

533 The total bone density, cortical bone density, and cancellous bone density of the femoral (A)  
534 distal epiphysis and (B) femoral midshaft were evaluated by pQCT. (C). The eccentricity and  
535 average fluorescence intensity of sclerostin on the anterior, posterior, lateral, and medial sides  
536 were quantified in the Sham and NX groups. The data of (A) and (B) and the lower panel of (C)  
537 are expressed as the mean  $\pm$  SD (n=5 for pQCT and n=4 for immunofluorescence imaging); the  
538 data of the eccentricity are presented by Tukey's box-and-whisker plot. ANOVA, analysis of  
539 variance; ※, Paired *t*-test; \*, uncorrected Fisher's LSD test with a single pooled variance  
540 followed by a two-way analysis of variance with the paired sample. ※\*, p <0.05; ※※, \*\*, p  
541 <0.01.

542 **Fig. 3** The number of sclerostin-positive osteocytes in the lateral region was evaluated.

543 (A). Confocal tiling images of the lateral region. The sections were immunostained for Scl  
544 (green), and nuclei were stained with DAPI (blue). The white dashed line indicates the border  
545 between the marrow and cortical bone. The alternate long- and short-dash line indicates the  
546 border between the periosteal and cortical bone. The area from the marrow side to the periosteal  
547 side of the cortical bone was divided into four regions: I, II, III, and IV. Scale bar=100  $\mu\text{m}$ . (B).



548 Magnified images of regions I, II, III, and IV. Scale bar =20  $\mu\text{m}$ . (C). The ratio of Scl-positive  
549 osteocytes to total osteocytes (nuclei stained with DAPI) in regions I, II, III, and IV. The data  
550 are expressed as the mean  $\pm$  SD (n=4). The asterisks indicate significant differences from the  
551 Sham group (\*,  $p < 0.05$ : paired *t*-test). (D). Three-dimensional immunofluorescence images of  
552 osteocytes in regions IV constructed using the IMARIS software program. Three-dimensional  
553 fluorescence images (upper figures) were constructed using the IMARIS software program.  
554 Surface rendering images corresponding to lower figures are shown. Scl and the nuclei are  
555 indicated in green and blue, respectively. Scale bar=10  $\mu\text{m}$ .

556 **Fig. 4** The Scl distribution inside the osteocyte cell body, lacuna, and canaliculi was evaluated by  
557 immunoelectron microscopy.

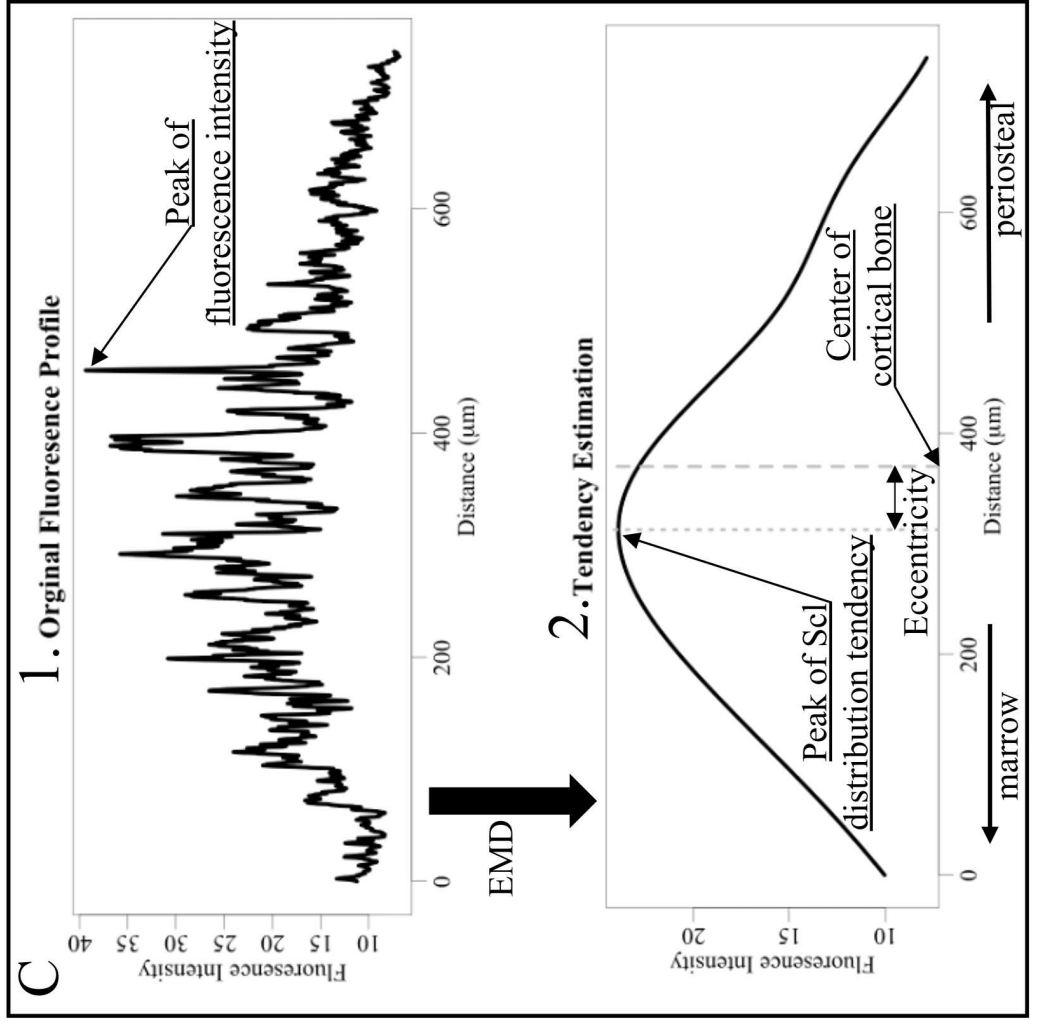
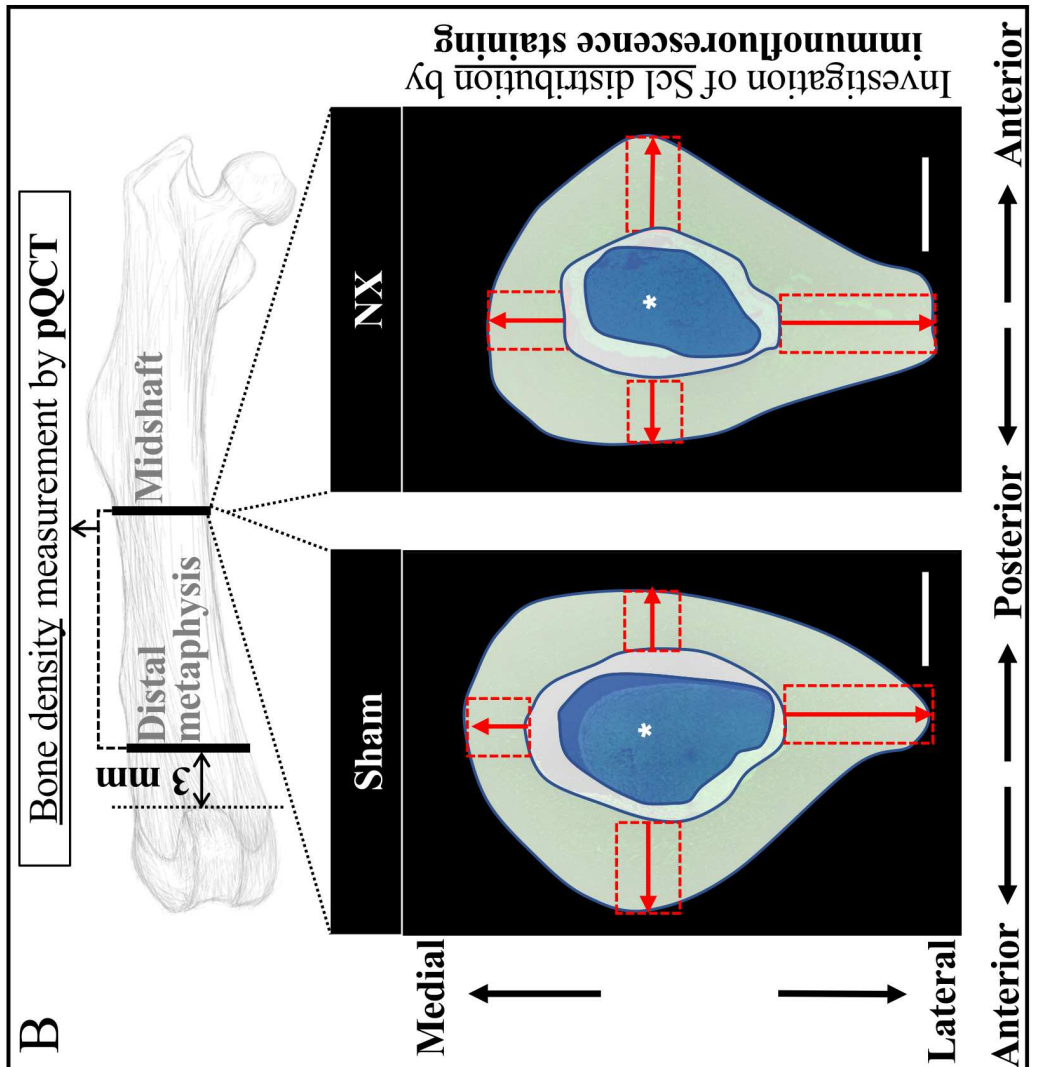
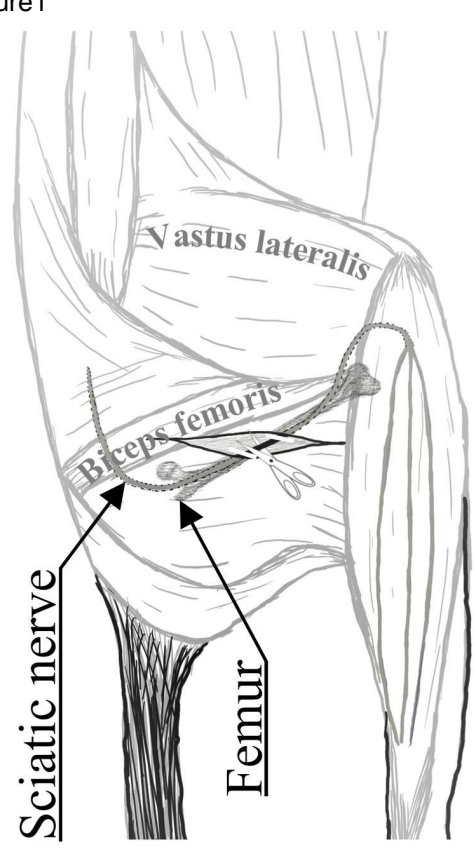
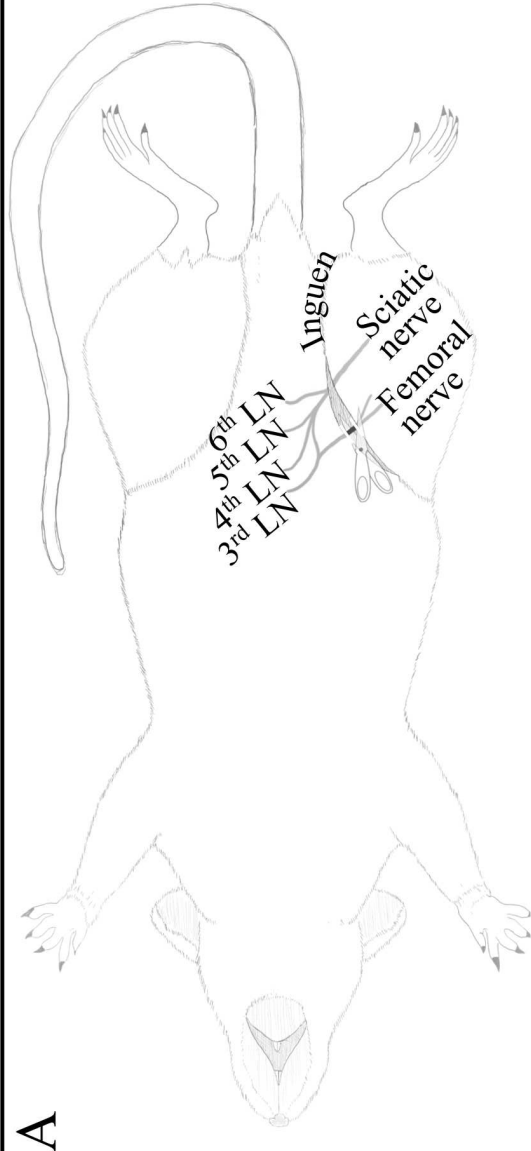
558 (A). The analysis of Scl labeled by 10-nm gold colloid using TEM in the lateral region. (a, b)  
559 TEM images. The red single-dot chain line indicates the border between the osteocyte cell body  
560 and lacuna. The blue dotted chain line indicates the border between the lacuna and bone matrix.  
561 The yellow double-dot chain line indicates the border between the canaliculi and the bone  
562 matrix. Scale bar=3  $\mu\text{m}$ . (c-f) Magnified images of the white square border. Scale bar=300 nm.  
563 (B). Scl density per unit area (upper panel) and the area (lower panel) of the osteocyte cell body,  
564 lacuna, and canaliculi. The data are expressed as the mean  $\pm$  SD (n=4); \*, uncorrected Fisher's  
565 LSD test with a single pooled variance followed by a two-way analysis of variance with the  
566 paired sample; \*,  $p < 0.05$ ; \*\*,  $p < 0.01$ .

567 **Online Resource 1.** A video to show that the entire target leg was fully immobilized.

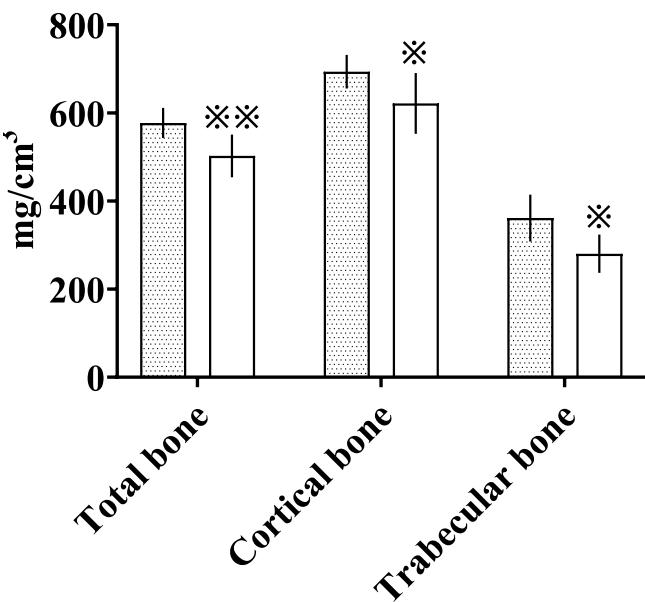
568 In this video, the rat was walking with a slow dragging motion without lifting the right foot. We  
569 shot this video one day after the excision of the sciatic and femoral nerves.



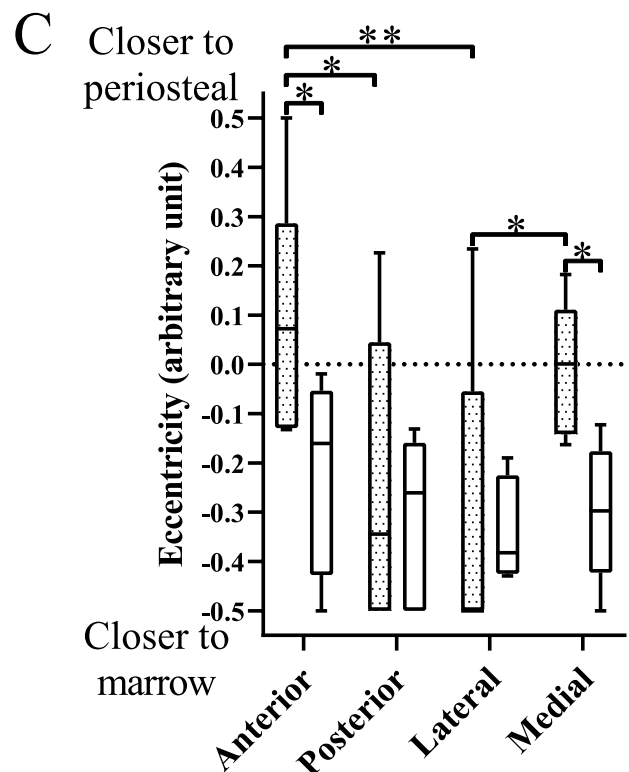
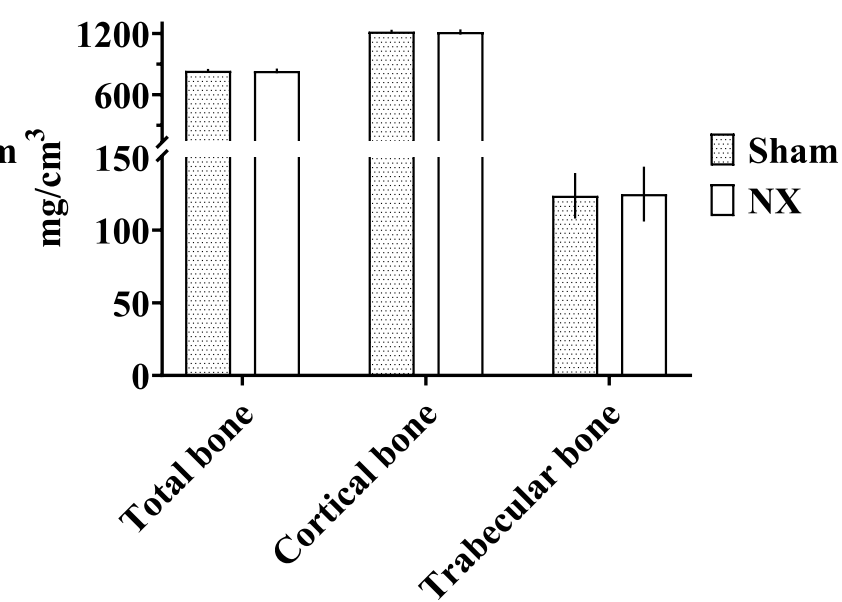
Figure 1



**Figure 2** Bone density of distal metaphysis

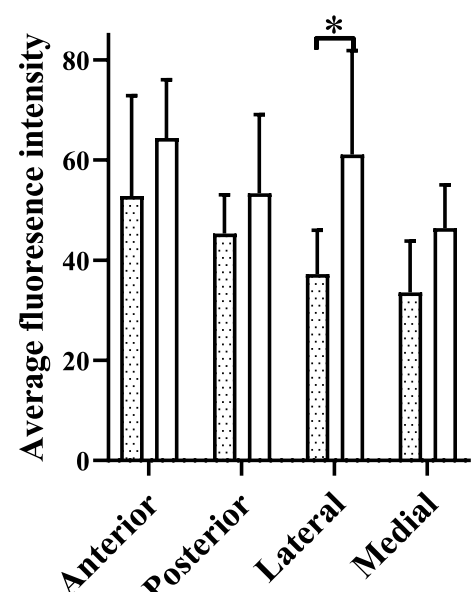


**B** Bone density of diaphysis



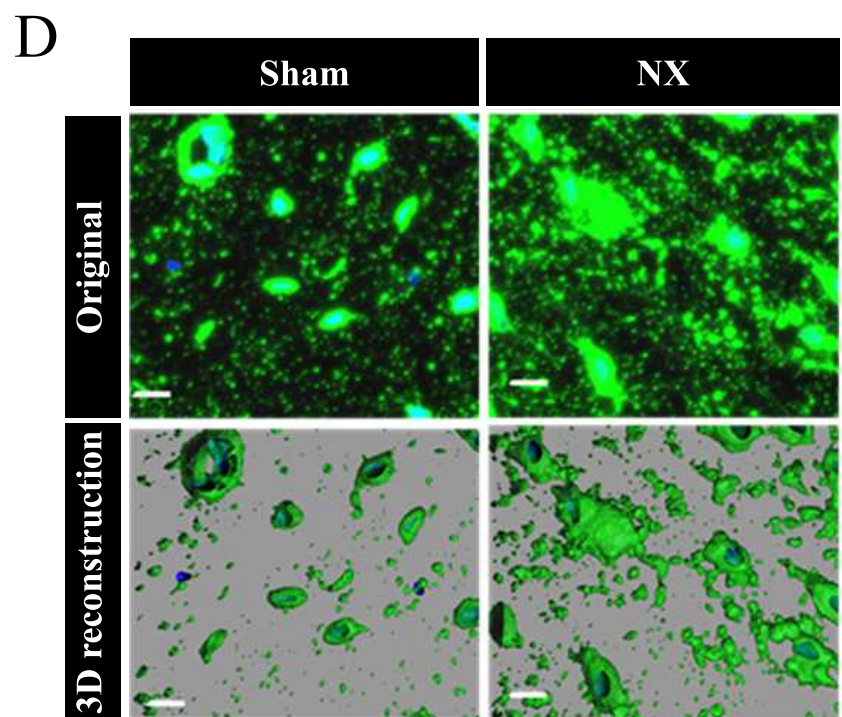
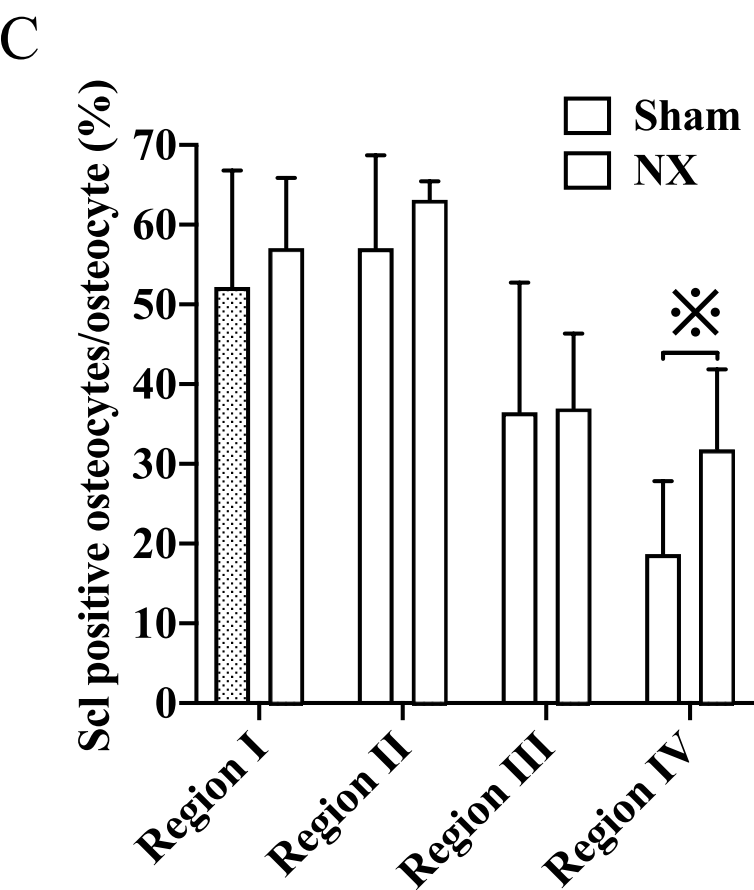
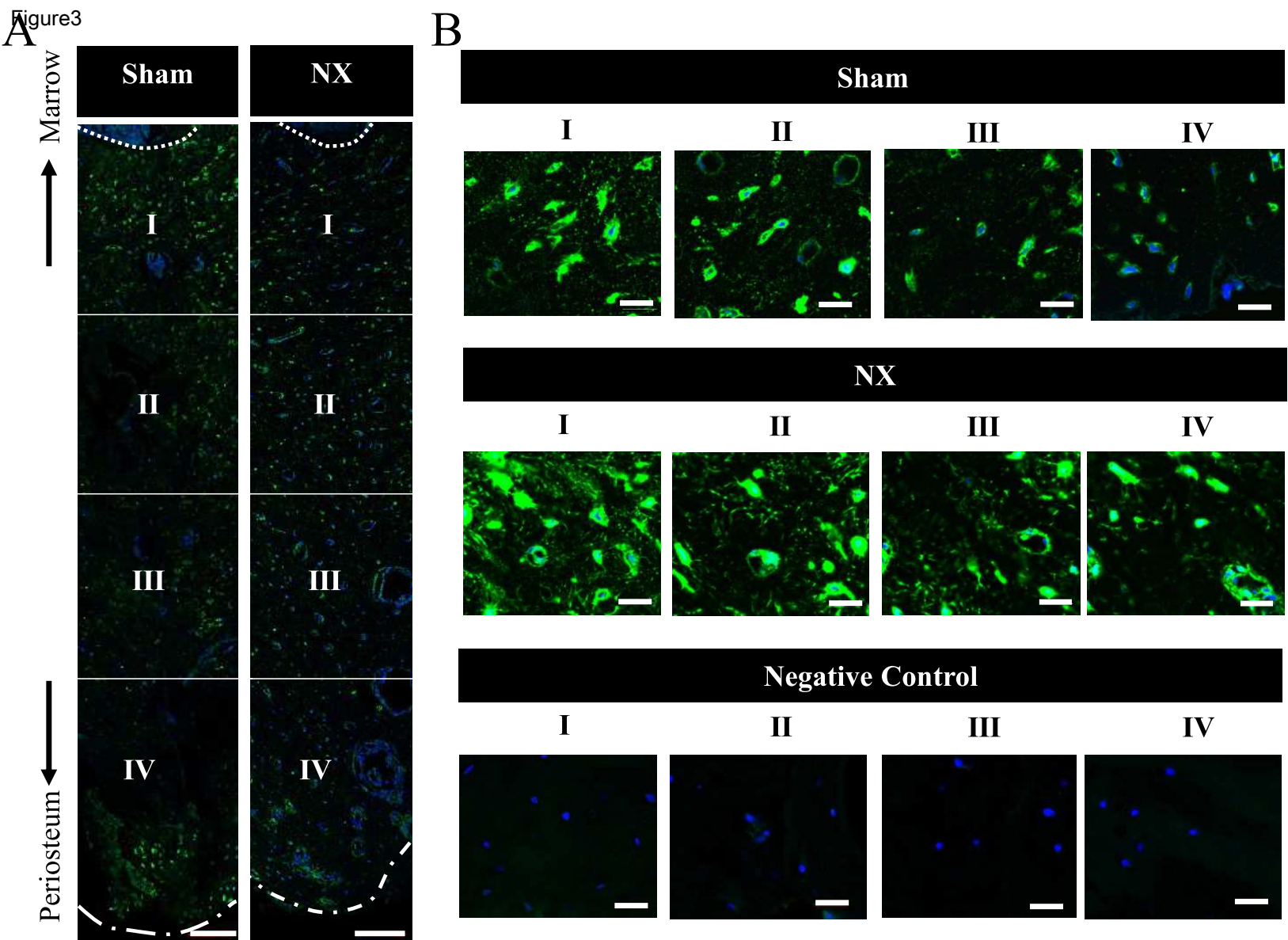
Two-way ANOVA

Source of Variation	Percentage of total variation (%)	P value
Interaction	6.964	0.3398
Position	17.31	0.0508
NX	11.74	<b>0.0212</b>



Two-way ANOVA

Source of Variation	Percentage of total variation (%)	P value
Interaction	3.57	0.6939
Position	17.65	0.0918
NX	20.18	<b>0.0083</b>



## Sham

## NX

